Research Article | Vol. 24, No. 23 | 14 Nov 2016 | OPTICS EXPRESS 26119

Optics EXPRESS

Characteristics of strain-sensitive photonic crystal cavities in a flexible substrate

YOU-SHIN NO, JAE-HYUCK CHOI, KYOUNG-HO KIM, AND HONG-GYU PARK*

Department of Physics, Korea University, Seoul 02841, South Korea
**hgpark@korea.ac.kr*

Abstract: High-index semiconductor photonic crystal (PhC) cavities in a flexible substrate support strong and tunable optical resonances that can be used for highly sensitive and spatially localized detection of mechanical deformations in physical systems. Here, we report theoretical studies and fundamental understandings of resonant behavior of an optical mode excited in strain-sensitive rod-type PhC cavities consisting of high-index dielectric nanorods embedded in a low-index flexible polymer substrate. Using the three-dimensional finite-difference time-domain simulation method, we calculated two-dimensional transverse-electric-like photonic band diagrams and the three-dimensional dispersion surfaces near the first Γ-point band edge of unidirectionally strained PhCs. A broken rotational symmetry in the PhCs modifies the photonic band structures and results in the asymmetric distributions and different levels of changes in normalized frequencies near the first Γ-point band edge in the reciprocal space, which consequently reveals strain-dependent directional optical losses and selected emission patterns. The calculated electric fields, resonant wavelengths, and quality factors of the band-edge modes in the strained PhCs show an excellent agreement with the results of qualitative analysis of modified dispersion surfaces. Furthermore, polarization-resolved time-averaged Poynting vectors exhibit characteristic dipole-like emission patterns with preferentially selected linear polarizations, originating from the asymmetric band structures in the strained PhCs.

OCIS codes: (050.6624) Subwavelength structures; (050.5298) Photonic crystals; (140.4780) Optical resonators; (050.1755) Computational electromagnetic methods.

References and links

1. M. J. Burek, Y. Chu, M. S. Z. Liddy, P. Patel, J. Rochman, S. Meesala, W. Hong, Q. Quan, M. D. Lukin, and M. Lončar, "High quality-factor optical nanocavities in bulk single-crystal diamond," Nat. Commun. **5**, 5718 (2014), doi:10.1038/ncomms6718.
2. B.-S. Song, S. Noda, T. Asano, and Y. Akahane, "Ultra-high-Q photonic double-heterostructure nanocavity," Nat. Mater. **4**(3), 207–210 (2005).
3. S. John, "Why trap light?" Nat. Mater. **11**(12), 997–999 (2012).
4. S.-H. Kwon, J.-H. Kang, C. Seassal, S.-K. Kim, P. Regreny, Y.-H. Lee, C. M. Lieber, and H.-G. Park, "Subwavelength plasmonic lasing from a semiconductor nanodisk with silver nanopan cavity," Nano Lett. **10**(9), 3679–3683 (2010).
5. S.-K. Kim, R. W. Day, J. F. Cahoon, T. J. Kempa, K.-D. Song, H.-G. Park, and C. M. Lieber, "Tuning light absorption in core/shell silicon nanowire photovoltaic devices through morphological design," Nano Lett. **12**(9), 4971–4976 (2012).
6. M. L. Brongersma, Y. Cui, and S. Fan, "Light management for photovoltaics using high-index nanostructures," Nat. Mater. **13**(5), 451–460 (2014).
7. T. Baba, "Slow light in photonic crystals," Nat. Photonics **2**(8), 465–473 (2008).
8. K. Nozaki, A. Shinya, S. Matsuo, Y. Suzaki, T. Segawa, T. Sato, Y. Kawaguchi, R. Takahashi, and M. Notomi, "Ultralow-power all-optical RAM based on nanocavities," Nat. Photonics **6**(4), 248–252 (2012).
9. E. Kuramochi, K. Nozaki, A. Shinya, K. Takeda, T. Sato, S. Matsuo, H. Taniyama, H. Sumikura, and M. Notomi, "Large-scale integration of wavelength-addressable all-optical memories on a photonic crystal chip," Nat. Photonics **8**(6), 474–481 (2014).
10. K.-Y. Jeong, Y.-S. No, Y. Hwang, K. S. Kim, M.-K. Seo, H.-G. Park, and Y.-H. Lee, "Electrically driven nanobeam laser," Nat. Commun. **4**, 2822 (2013), doi:10.1038/ncomms3822.

#276514 http://dx.doi.org/10.1364/OE.24.026119
Journal © 2016 Received 23 Sep 2016; revised 27 Oct 2016; accepted 28 Oct 2016; published 1 Nov 2016

Optics EXPRESS

11. D. Englund, A. Faraon, I. Fushman, N. Stoltz, P. Petroff, and J. Vucković, "Controlling cavity reflectivity with a single quantum dot," Nature **450**(7171), 857–861 (2007).
12. P. Jing, J. Wu, and L. Y. Lin, "Patterned optical trapping with two-dimensional photonic crystals," ACS Photonics **1**(5), 398–402 (2014).
13. M. R. Lee and P. M. Fauchet, "Two-dimensional silicon photonic crystal based biosensing platform for protein detection," Opt. Express **15**(8), 4530–4535 (2007).
14. G. Shambat, S.-R. Kothapalli, J. Provine, T. Sarmiento, J. Harris, S. S. Gambhir, and J. Vučković, "Single-cell photonic nanocavity probes," Nano Lett. **13**(11), 4999–5005 (2013).
15. X. Gan, H. Clevenson, C.-C. Tsai, L. Li, and D. Englund, "Nanophotonic filters and integrated networks in flexible 2D polymer photonic crystals," Sci. Rep. **3**, 2145 (2013).
16. W. Zhou, Z. Ma, H. Yang, Z. Qiang, G. Qin, H. Pang, L. Chen, W. Yang, S. Chuwongin, and D. Zhao, "Flexible photonic-crystal Fano filters based on transferred semiconductor nanomembranes," J. Phys. D Appl. Phys. **42**(23), 234007 (2009).
17. T.-W. Lu, L.-H. Chiu, P.-T. Lin, and P.-T. Lee, "One-dimensional photonic crystal nanobeam lasers on a flexible substrate," Appl. Phys. Lett. **99**(7), 071101 (2011).
18. X. Xu, H. Subbaraman, S. Chakravarty, A. Hosseini, J. Covey, Y. Yu, D. Kwong, Y. Zhang, W.-C. Lai, Y. Zou, N. Lu, and R. T. Chen, "Flexible single-crystal silicon nanomembrane photonic crystal cavity," ACS Nano **8**(12), 12265–12271 (2014).
19. C. L. Yu, H. Kim, N. de Leon, I. W. Frank, J. T. Robinson, M. McCutcheon, M. Liu, M. D. Lukin, M. Loncar, and H. Park, "Stretchable photonic crystal cavity with wide frequency tunability," Nano Lett. **13**(1), 248–252 (2013).
20. M.-H. Shih, K.-S. Hsu, K. Lee, K.-T. Lai, C.-T. Lin, and P.-T. Lee, "Compact tunable laser with InGaAsP photonic crystal nanorods for C-band communication," IEEE J. Sel. Top. Quantum Electron. **21**, 4900505 (2015).
21. J.-H. Choi, Y.-S. No, J.-P. So, J. M. Lee, K.-H. Kim, M.-S. Hwang, S.-H. Kwon, and H.-G. Park, "A high-resolution strain-gauge nanolaser," Nat. Commun. **7**, 11569 (2016), doi:10.1038/ncomms11569.
22. J.-H. Choi, Y.-S. No, M.-S. Hwang, S.-Y. Kwon, K.-Y. Jeong, S.-H. Kwon, J.-K. Yang, and H.-G. Park, "Low-threshold photonic-band-edge laser using iron-nail-shaped rod array," Appl. Phys. Lett. **104**(9), 091120 (2014).
23. X. Letartre, J. Mouette, J. L. Leclercq, P. R. Romeo, C. Seassal, and P. Viktorovitch, "Switching devices with spatial and spectral resolution combining photonic crystal and MOEMS structures," J. Lightwave Technol. **21**(7), 1691–1699 (2003).
24. B. B. Bakir, C. Seassal, X. Letartre, P. Viktorovitch, M. Zussy, L. D. Cioccio, and J. M. Fedeli, "Surface-emitting microlaser combining two-dimensional photonic crystal membrane and vertical Bragg mirror," Appl. Phys. Lett. **88**(8), 081113 (2006).
25. L. Ferrier, P. Rojo-Romeo, E. Drouard, X. Letatre, and P. Viktorovitch, "Slow Bloch mode confinement in 2D photonic crystals for surface operating devices," Opt. Express **16**(5), 3136–3145 (2008).
26. L. Ferrier, O. El Daif, X. Letartre, P. Rojo Romeo, C. Seassal, R. Mazurczyk, and P. Viktorovitch, "Surface emitting microlaser based on 2D photonic crystal rod lattices," Opt. Express **17**(12), 9780–9788 (2009).
27. K. Sakai and S. Noda, "Optical trapping of metal particles in doughnut-shaped beam emitted by photonic-crystal laser," Electron. Lett. **43**(2), 107 (2007).
28. T.-P. Vo, A. Rahmani, A. Belarouci, C. Seassal, D. Nedeljkovic, and S. Callard, "Near-field and far-field analysis of an azimuthally polarized slow Bloch mode microlaser," Opt. Express **18**(26), 26879–26886 (2010).
29. K. Sakai, E. Miyai, T. Sakaguchi, D. Ohnishi, T. Okano, and S. Noda, "Lasing band-edge identification for a surface-emitting photonic crystal laser," IEEE J. Sel. Areas Comm. **23**(7), 1335–1340 (2005).

1. Introduction

Optical nanocavities that enable strong light confinement are promising building blocks for photonic circuits and optoelectronic devices, as well as for biological and chemical applications [1–14]. Photonic crystal (PhC) nanocavities are of particular interest because rational design and engineering of photonic band structures allow efficient manipulation of light and its interaction with matter. Integrated on-chip photonic networks, coupled cavity quantum electrodynamic systems, nanoscale optical tweezers, and bioprobes have been reported [7–14]. Recently, these unique features of PhC nanocavities were combined with rapid advances in flexible technologies, opening up unprecedented opportunities for optical monitoring of environmental changes in physical systems [15–21]. For example, high-index semiconductor rod-type PhCs embedded in a flexible substrate have demonstrated robust structural reconfigurability and repeatedly reversible wavelength tuning in response to applied strains [19–21]. A strain-gauge nanolaser has experimentally demonstrated the instantaneous optical visualization of the signs of strain and potential for mechanical strain-based tunable laser pH detection [21]. However, fundamental understanding of the underlying mechanisms

Optics EXPRESS

of engineered optical properties of strain-sensitive PhC cavities is still necessary for further practical applications.

In this work, we theoretically study strain-dependent optical properties of resonant modes excited in high-index rod-type PhC cavities embedded in a flexible substrate. The calculated three-dimensional dispersion characteristics of positively and negatively strained PhCs reveal the asymmetric nature of wavevector distributions and optical confinement in lateral directions, which leads to the selected emission patterns and directional optical losses. In addition, numerical simulations of electric fields, resonant wavelengths, quality factors, and polarization-resolved Poynting vectors quantitatively exhibit modal characteristics of the strained PhCs, supporting the analysis of engineered photonic band structures.

2. Results and discussion

Our strain-sensitive PhC structures are schematically shown in Fig. 1(a). An array of high-index dielectric nanorods with circular cross-sections forms square lattice PhCs. A transparent low-index viscoelastic polymer material uniformly covers the PhC structure to provide a flexible platform. In the rod-type PhCs, strong optical confinement can be achieved by taking advantage of photonic band edges in the transverse-electric-like (TE-like) photonic band structures at the Γ-point ($k_x = 0$, $k_y = 0$) [20–22]. Figure 1(b) shows the TE-like photonic band structures of rod-type square lattice PhCs, calculated using a finite-difference time-domain (FDTD) simulation method. In simulation, we employed InGaAsP and polydimethylsiloxane (PDMS) for high-index dielectric nanorods and a low-index flexible surrounding medium, respectively. The refractive indices of InGaAsP and PDMS were set to 3.4 and 1.4. The lattice constant was 650 nm. The radius and thickness of an individual nanorod were 250 and 250 nm, respectively [inset, Fig. 1(b)]. Notably, one can obtain a highly symmetric and flat dispersion at the first Γ-point band edge. The flat dispersion curve near the band edge reveals a very low group velocity of light, which enables strong photon confinement within the nanostructures and subsequently supports a high-quality optical mode, called a band-edge mode [20–22]. The normalized frequency at the first Γ-point band edge is determined by the structural parameters of the nanorods. Varying the lattice constant severely changes the frequency of the band-edge mode; this dependence can be utilized for measuring the mechanical strain or structural deformation in the PhC structures [20,21]. Combining high-index nanorods with a flexible material is useful for demonstrating strain-sensitive tunable PhC cavities with high flexibility and reversibility.

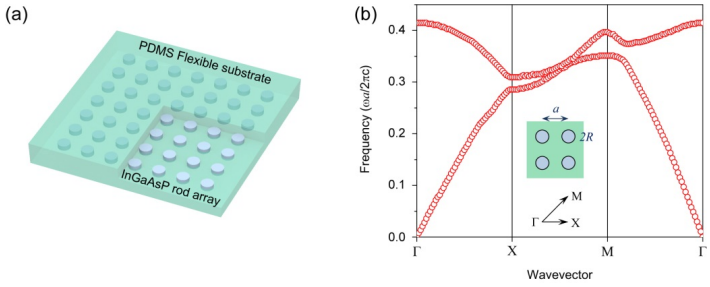

Fig. 1. Strain-sensitive flexible PhC structures and representative photonic band diagram. (a) Schematic illustration exhibiting rod-type square lattice PhCs in a flexible substrate. High-index InGaAsP semiconductor nanorods (light blue) are embedded in a low-index flexible PDMS polymer substrate (cyan). (b) The calculated TE-like photonic band diagram of the PhC structure in (a). The lattice constant (a in the inset) was 650 nm and the radius of an individual rod (R in the inset) was 250 nm. For each rod the thickness was 250 nm. The x-axis is the wavevector, and the y-axis is normalized frequency in the units of $\omega a/2\pi c$, where ω is the angular frequency in free space and c is the speed of light.

To characterize the band-edge mode in the rod-type PhCs with structural deformations, we systematically varied the lattice constant of PhCs in one direction and investigated the

Optics EXPRESS

characteristics of TE-like photonic band structures near the first Γ-point band edge. Figure 2(a) schematically shows rod-type PhCs under three different strain conditions, while Fig. 2(b) shows the respective TE-like three-dimensional dispersion surfaces near the first Γ-point band edge. In these simulations, the same structural parameters of nanorods as those in Fig. 1 were used. The PhCs were compressed [Fig. 2(a), left], pristine [Fig. 2(a), middle], or stretched [Fig. 2(a), right] in one direction (*y*-direction), but no deformation was applied in the other direction (*x*-direction). To realize these structural alterations, we only varied the lattice constant in the *y*-direction, a_y, setting it to 550, 650, and 750 nm, respectively. The lattice constant in the *x*-direction, a_x, was fixed at 650 nm. Consequently, the simulated PhC structures were subjected to the negative (–15.4%), pristine (0.0%), and positive (15.4%) strains. Here, the applied strains were calculated by normalizing a_y for all PhCs with respect to the a_y value for pristine PhCs (650 nm). We then calculated the normalized frequency of the resonant band-edge mode near the first Γ-point band edge as we varied the k_x and k_y wavevectors in the reciprocal (or momentum) space from –0.1 to 0.1. Figure 2(b) shows three-dimensional dispersion surfaces obtained for the negative [Fig. 2(b), left], pristine [Fig. 2(b), middle], and positive [Fig. 2(b), right] strain conditions.

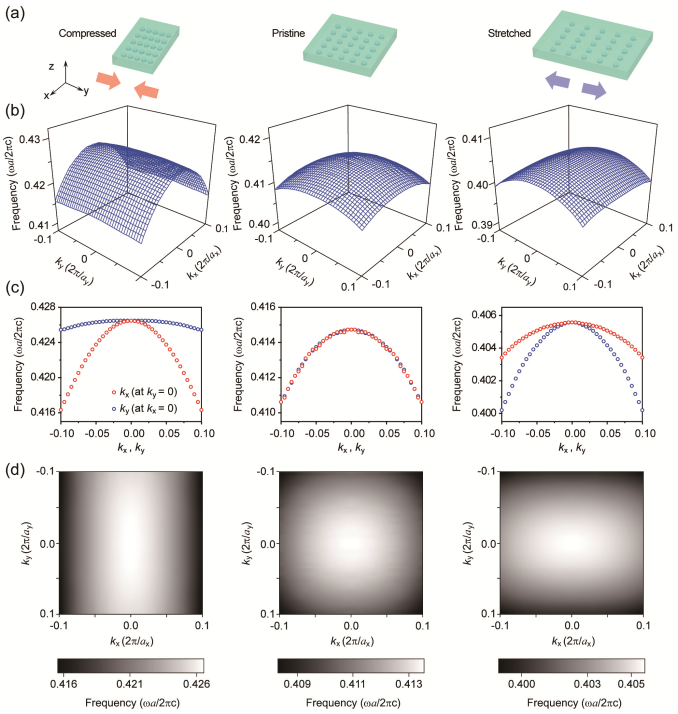

Fig. 2. Strain-sensitive photonic band structures of the simulated PhCs, for different strain conditions. (a) Schematics of structural changes in the simulated PhCs subject to negative (left), pristine (middle), and positive (right) strains. Strains were applied in the *y*-direction only. (b) Three-dimensional transverse-electric-like dispersion surfaces were calculated near the first Γ-point band edge, for the negative (left), pristine (middle), and positive (right) strains. The lattice constant in the *x*-direction (a_x) in PhCs was fixed at 650 nm for all strain conditions, while the lattice constants in the *y*-direction (a_y) was set to 550, 650, and 750 nm, to simulate negative (–15.4%), pristine (0.0%), and positive (15.4%) strains. The normalized frequency was calculated as both k_x and k_y were varied from –0.1 to 0.1. Here, k_x and k_y are wavevectors in the units of $2\pi/a_x$ and $2\pi/a_y$, respectively. The radii and the thicknesses of all the nanorods were the same as those in Fig. 1(b). (c) Corss-sectional plots of (b) for negatively (left), pristine (middle) and positively (right) strained PhC structures when k_x (k_y) varied from –0.1 to 0.1 for a fixed k_y = 0.0 (k_x = 0.0). (d) Two-dimensional color maps of the dispersion surfaces near the first Γ-point, shown in (b). Color bar in each two-dimensional map is normalized with the maximal normalized frequency at the Γ-point.

Optics EXPRESS

The dispersion surfaces of the simulated strained PhCs exhibit the following key features. First, the resonant frequency of the band-edge mode at the Γ-point (k_x = 0, k_y = 0) increased (decreased) from 0.4147 to 0.4265 (0.4056) when the negative (positive) strain was applied to the PhCs [Fig. 2(c)]. Decreased (increased) lattice constant in the PhC structure allows the excitation of the band-edge mode with an increased (decreased) resonant frequency [20,21]. Second, unidirectional strain broke the system's C_4 rotational symmetry (invariant under the 90° rotation around the z-axis) at the Γ-point and produced the C_2 rotational symmetry (invariant under 180° rotation around the z-axis), changing the photonic band structures near the Γ-point. For example, the normalized frequency changed rapidly and resulted in a large difference of resonant wavelengths, $\Delta\lambda$, of ~37.2 nm (~21.5 nm) when k_x (k_y) varied from ± 0.1 to 0.0 for a fixed k_y = 0.0 (k_x = 0.0) in the negatively (positively) strained PhCs [Figs. 2(b)–2(c)]. On the other hand, the normalized frequency changed relatively weakly and resulted in a relatively small $\Delta\lambda$ of ~3.7 nm (~8.5 nm) when k_y (k_x) varied from ± 0.1 to 0.0 for a fixed k_x = 0.0 (k_y = 0.0) in the negatively (positively) strained PhCs. Third, dispersion curves along the k_y (k_x) direction for a fixed k_x (k_y) became more flattened compared with those for the pristine PhCs, in response to the negative (positive) strain [Figs. 2(b)–2(c)]. In Fig. 2(d), we clearly visualized these features by converting the three-dimensional dispersion surfaces into two-dimensional frequency color plots. In these plots, an asymmetric nature of each photonic band structure around the first Γ-point band edge for the strained PhCs becomes more pronounced. For example, the band structure of the negatively strained PhCs [Fig. 2(d), left] demonstrates a stronger asymmetry and larger difference between the resonant frequencies at the Γ-point and corners (k_x = ± 0.1 or k_y = ± 0.1) compared with the positively strained PhCs [Fig. 2(d), right]. In addition, the x-component (y-component) of the group velocity, $v_x = \partial\omega/\partial k_x \mid k_y = 0$ ($v_y = \partial\omega/\partial k_y \mid k_x = 0$), of the negatively (positively) strained PhCs strongly differs from that of the pristine PhCs near the Γ-point, whereas $v_y \mid k_x = 0$ ($v_x \mid k_y = 0$) exhibits relatively less noticeable variations.

In fact, the above observations are useful for understanding the lateral confinement and optical loss of band-edge modes when the size of the strained PhCs becomes finite. For two-dimensional finite-size PhCs the wavevector **k** is not definite at the Γ-point but has an extent $\Delta\mathbf{k}$. In this case, the dispersion relation is approximately $\omega = \omega_0 + \alpha k_{\parallel}^2/2$, where $k_{\parallel}$ is the lateral wavevector ($k_{\parallel}^2 = k_x^2 + k_y^2$) and α is the second derivative of the dispersion (the curvature of the band). The group velocity is also expressed as $\mathbf{v}_g = d\omega/d\mathbf{k} = \alpha k_{\parallel}$ [23–26]. Then, the lateral optical loss is described as $1/Q_{\text{lateral}} = 1/\omega\tau = 1/(\omega_0 + \alpha k_{\parallel}^2/2)\tau$, where Q_{lateral} and τ are the quality factor in the lateral direction and the photon life time in the finite-size PhCs, respectively [24,25]. Therefore, the observed asymmetric curvatures in photonic band structures near the Γ-point can partially explain the confinement mechanism and optical loss in strained finite-size PhCs [24,25]. For example, the band-edge mode in negatively (positively) strained finite-size PhCs can experience less confinement in the x-direction (y-direction) owing to the greater curvature of its three-dimensional dispersion surface compared with pristine PhCs. Subsequently, the optical loss in that direction can be more dominant. Taken together, the studies of photonic band structures and resulting observations can provide important clues for further understanding the origins of modified optical properties of band-edge modes, such as mode quality factors and near- and far-field emission patterns.

Optics EXPRESS

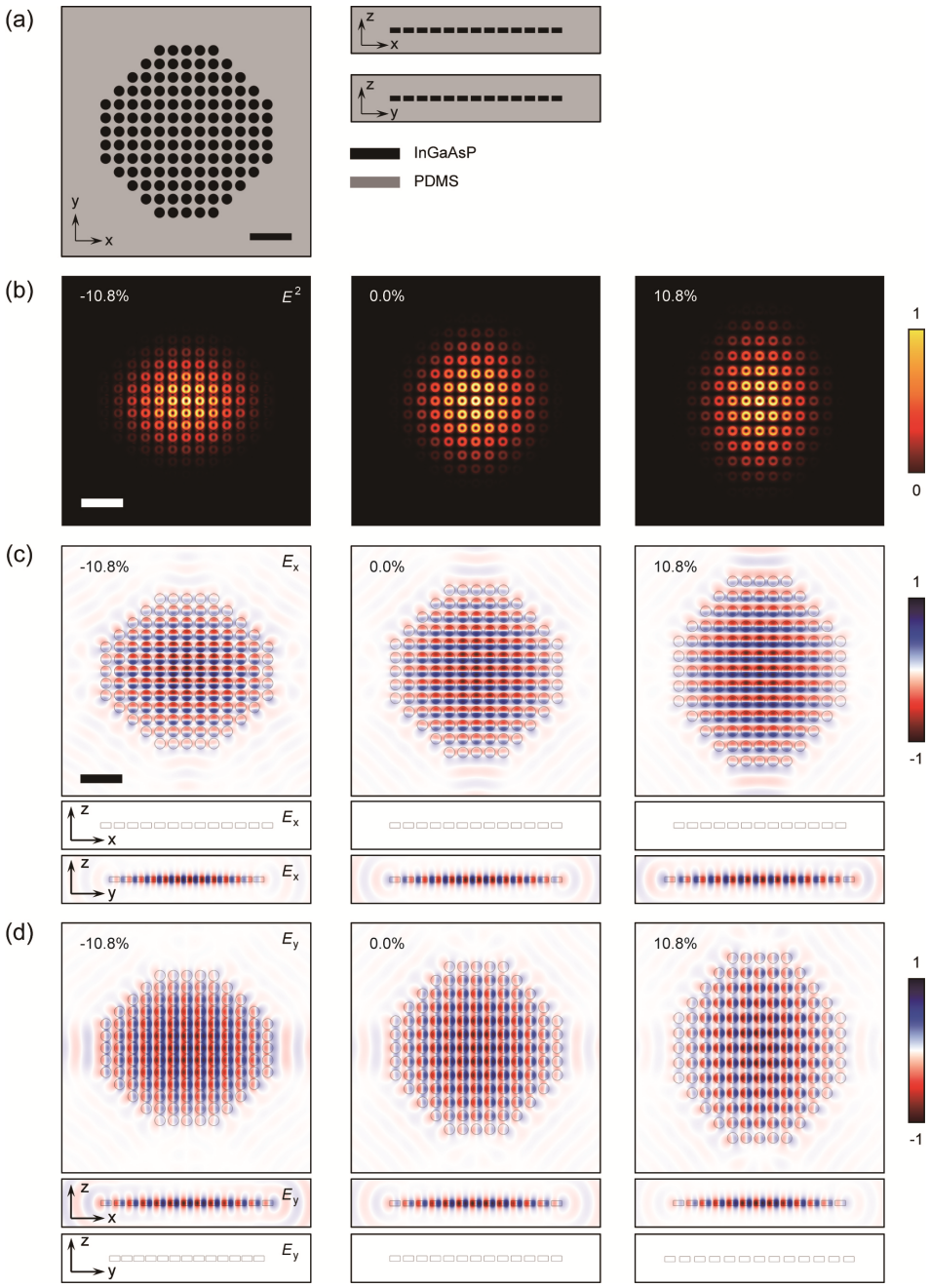

Fig. 3. Electric field components and intensity profiles in finite-size PhC band-edge cavities under different strains. (a) Simulated structures showing top (left) and side (right) views of a square lattice of finite-size PhC band-edge cavity. An array of InGaAsP nanorods (black) in a 13 × 13 grid layout with a circular outer boundary is embedded in a PDMS (light brown) substrate. The lattice constant and radii of individual nanorods are 650 and 250 nm, respectively. The rod thickness is 250 nm. The scale bar is 2 μm. (b)–(d) The calculated electric field components and intensity profiles of the Γ-point band-edge mode in PhC cavities, for negative (–10.8%, left column), pristine (0.0%, middle column), and positive (10.8%, right column) strains. Strains were applied in the *y*-direction. All profiles were normalized by their maxima. In all panels the scale bar is 2 μm.

Optics EXPRESS

Based on the fundamental understanding of the first Γ-point band-edge mode in Fig. 2, we further investigated the optical properties of the band-edge mode in strained PhCs by performing full three-dimensional FDTD simulations. For practicality, we considered a square lattice of finite-size rod-type PhC structures [Fig. 3]. An array of InGaAsP nanorods [Fig. 3(a), black circular dots] within a circular outer boundary with a radius of 6*a*, where *a* is the lattice constant, was embedded in a PDMS flexible substrate [Fig. 3(a), grey background] [21,22]. The lattice constant, the radius and the thickness of the nanorods were 650, 250, and 250 nm, respectively. In Figs. 3(b)–3(d), we applied negative (−10.8%, left), pristine (0.0%, middle) and positive (10.8%, right) strains to the PhCs in the *y*-direction using the way described above, and calculated electric field and intensity distributions. We observed concentration of strong electric fields at individual nanorods, with a central intensity minimum for all PhCs [Fig. 3(b)]. The overall intensity profiles depended on structural alterations and exhibited an elliptical shape along the *x*-direction (*y*-direction) for the negatively (positively) strained PhCs. We also calculated the *x*-component (E_x) and *y*-component (E_y) of electric fields, for each strained PhCs [Figs. 3(c)–3(d)]. As predicted in Fig. 2, we observed a noticeable leak of the electric fields toward lateral directions. Specifically, the leakage occurred along the preferential directions depending on the sign of the strains. For example, when the negative (positive) strain was applied to PhCs, a portion of the E_y-fields (E_x-fields) dominantly propagated in the *x*-direction (*y*-direction) out of the array of PhC nanorods [Figs. 3(c)–3(d), left and right]. There was a relatively small (or negligible) propagation of the electric fields in the other direction. We also observed different levels of directional leakage in the positively vs. negatively strained finite-size PhCs, which can be partially explained by the two different curvatures in the modified band structures [Figs. 2(b)–2(d)]. On the other hand, for the pristine PhCs the electric fields propagated equally in both directions [Figs. 3(c)–3(d), middle].

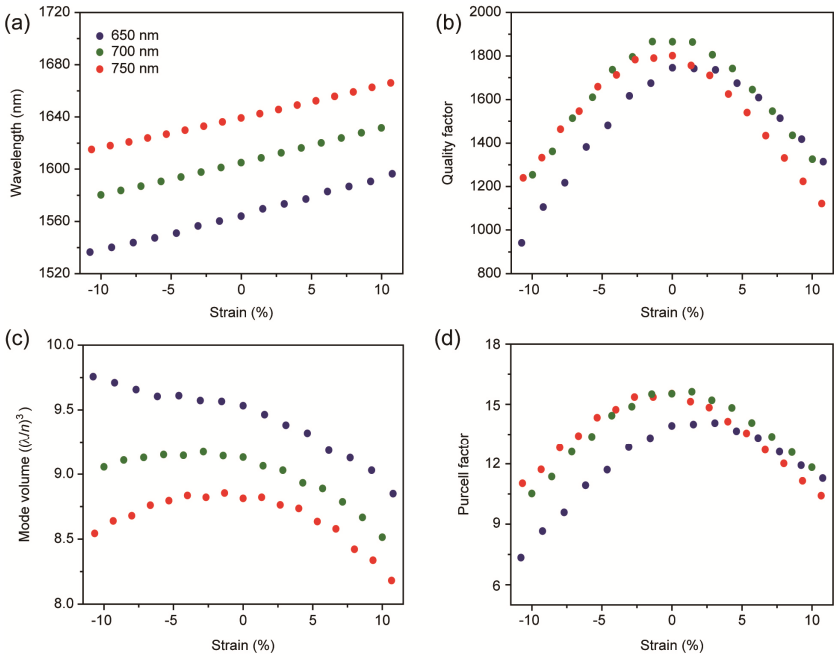

Fig. 4. Optical properties of the band-edge mode in finite-size PhC band-edge cavities under different strains. (a)–(d): calculated resonant wavelengths (a), quality factors (b), mode volumes (c), and Purcell factors (d) of the Γ-point band-edge mode, plotted vs. the applied strain. PhC structures with intrinsic lattice constants of 650 (blue), 700 (green), and 750 nm (red) were simulated.

Optics EXPRESS

We further employed various PhC structures with different lattice constants (650, 700, and 750 nm) and systematically changed the applied strain from negative to positive in the *y*-direction. Subsequently, we calculated the resonant wavelengths [Fig. 4(a)] and corresponding quality factors [Fig. 4(b)] of the band-edge modes. The resonant wavelength linearly increased (decreased) as the positive (negative) strain was applied to the PhCs. In addition, the linear scaling nature of PhCs and photonic band structure yielded a nearly constant shift in the resonant wavelength as the lattice constant was varied from 650 to 750 nm. In Fig. 4(b), the quality factor of the band-edge mode decreased when positive or negative strains were applied. In particular, a sharp reduction was observed for the negative strain, compared with the one obtained for the positive strain, when the lattice constant was 650 nm. The modifications of dispersion surfaces for strained PhCs can partially explain this trend of the quality factor: the different sign but same magnitude of applied strains can cause different levels of modifications of the three-dimensional dispersion surfaces near the first Γ-point. Consequently, the curvature near the Γ-point is likely to be more significant for negatively strained PhCs, causing the light to propagate in the lateral direction, in turn yielding a more significant optical loss in the band-edge mode [24,25]. We note that different trends of quality factors were observed at the increased lattice constants of 700 and 750 nm [Fig. 4(b)]. For example, the simulation result showed the maximal quality factor in slight negative strain at a lattice constant of 750 nm, whereas it was in slight positive strain at a lattice constant of 650 nm.

For more quantitative characterization, we calculated mode volumes in the unit of $(\lambda/n)^3$, where λ is the resonant wavelength and n is the refractive index of InGaAsP [Fig. 4(c)], and estimated the Purcell factors of the band-edge modes [Fig. 4(d)]. When the lattice constant of PhCs was 650 nm, the calculated mode volumes in the unit of μm^3 varied slightly in response to the strain because of the intrinsic nature of band-edge mode whose field profile is distributed over the entire range of PhC patterns. However, after normalizing by the resonant wavelength, the mode volume decreased with increasing the applied strain, owing to the linearly increasing resonant wavelength [Fig. 4(c)]. For the increased lattice constants of 700 and 750 nm, the mode volumes depend on the structural changes more significantly, and decrease in the unit of μm^3 particularly in the negative strains. In addition, the Purcell factors, a measure of the enhancement of spontaneous emission rate by the optical environment [15], followed the trend that was observed for the quality factors versus the strain [Fig. 4(b)]. Detailed and quantitative modal properties, plotted as a function of the applied strain in Fig. 4, show an excellent agreement with the observations and analyses in Fig. 2 and strongly support our understanding of photonic band structures [24,25].

Optics EXPRESS

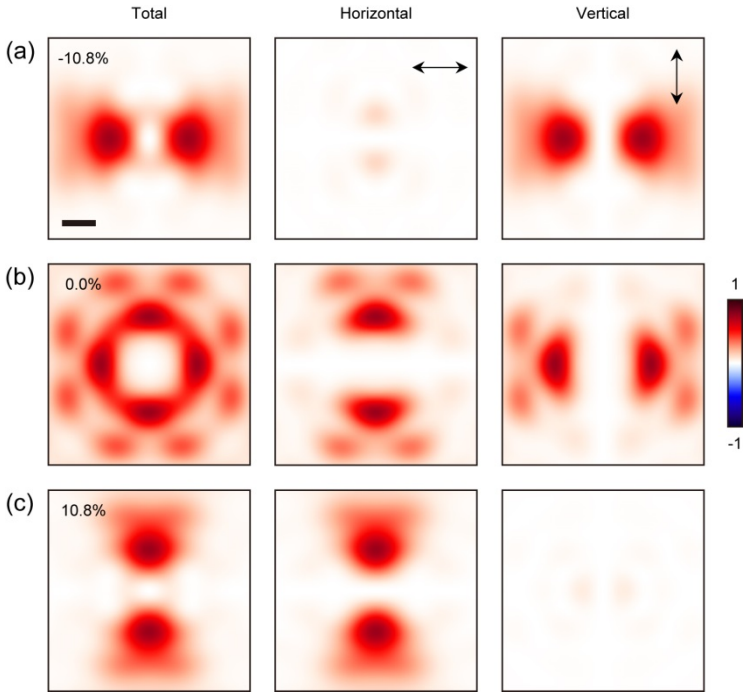

Fig. 5. Polarization properties of the band-edge modes in strained PhC cavities. (a)–(c) The *z*-components of total (<S_z>, left column) and horizontally- (<E_xH_y>, middle column) and vertically-polarized (<$-H_xE_y$>, right column) time-averaged Poynting vector distributions of the Γ-point band-edge modes in PhC cavities, for the negative (a, −10.8%), pristine (b, 0.0%) and positive (c, 10.8%) strain conditions. An H_z dipole source was introduced at the center of the PhCs to excite the Γ-point band-edge mode. The strain direction is the same as in Fig. 3. These distributions were obtained at a position 14 μm above the top surface of the array of InGaAsP nanorods. The Poynting vectors were normalized by their maxima. The scale bar is 2 μm.

Finally, we have studied the characteristics of emission patterns of the band-edge modes in strained PhCs. Negative [Fig. 5(a), −10.8%], pristine [Fig. 5(b), 0.0%], and positive [Fig. 5(c), 10.8%] strains were applied to the PhCs, and the *z*-components of total [Fig. 5, left column] and horizontally- [Fig. 5, middle column] and vertically-polarized [Fig. 5, right column] time-averaged Poynting vectors were calculated. These Poynting vector distributions were obtained at the *z*-direction distance of 14 μm away from the array of InGaAsP nanorods. All Poynting vectors were normalized by their maxima. The same structural and material parameters as in Fig. 3(b) were used in these simulations.

When no strain was applied to the PhCs, the *z*-component of time-averaged Poynting vector distribution clearly exhibited a doughnut-shaped emission pattern with a central intensity node [Fig. 5(b), left], which is characteristic of a non-degenerate Γ-point band-edge mode [22,26–29]. Such a doughnut-shaped emission pattern is known to have an azimuthal polarization because it consists of the coherent superposition of two Hermite-Gaussian (HG) modes; HG_{10} with horizontal polarization and HG_{01} with vertical polarization [27–29]. Therefore, when calculating horizontally-polarized (vertically-polarized) time-averaged Poynting vectors, only the HG_{10} (HG_{01}) mode was selected [Fig. 5(b), middle and right]. However, when the negative (positive) strain was applied to the PhCs in the *y*-direction, the broken rotational symmetry in the PhC structure yielded a modal symmetry breaking and destructive interference in the horizontally-polarized (vertically-polarized) mode. As a result, we observed a linearly polarized dipole-shaped emission pattern with an intensity minimum along the direction parallel (perpendicular) to the strain [Figs. 5(a) and 5(c)]. Interestingly, the

Optics EXPRESS

axis of asymmetry in the modified photonic band structure in the reciprocal space corresponded to the axis of linear polarization in the Poynting vector distributions in the strained PhCs. Therefore, one can utilize these different mode emission patterns as a direct visual response for identifying the signs of strain and an overall shape of the modified photonic band structure near the Γ-point. In addition, since strain-sensitive PhCs produce emission patterns with linear and azimuthal polarizations, these structures can be used as unique light sources capable of selecting a desired wavelength and polarization.

3. Conclusion

In summary, we theoretically studied the underlying mechanisms of resonant behavior in strain-sensitive flexible PhC cavities consisting of InGaAsP nanorods uniformly covered with a PDMS substrate. The calculated three-dimensional dispersion surfaces near the first Γ-point band-edge of strained PhCs in one direction revealed that the broken C_4 rotational high symmetry in the PhCs modified the photonic band structures and resulted in both the asymmetric distributions and different levels of changes of normalized frequencies near the first Γ-point band edge in the reciprocal space. As a result, the components of group velocities near the band edge became unbalanced, giving rise to strain-dependent directional optical losses and selected emission patterns. Electric field components and intensity profiles together with quality factors of the band-edge modes in strained PhCs strongly supported the qualitative analysis of the modified dispersion surfaces. The polarization-resolved time-averaged Poynting vectors exhibited horizontally- or vertically-polarized dipole-like emission patterns for strained PhCs, whereas the emission pattern is azimuthally-polarized and doughnut-shaped for pristine PhCs. We believe that the presented results and understanding will be useful for a variety of applications of strain-sensitive PhCs cavities in physical, chemical, and biological systems. The insights generated by the present study are likely to be important for designing novel flexible photonic devices containing increasingly complex optical elements.

Funding

National Research Foundation of Korea (NRF) grant funded by the Korean government (MSIP) (No. 2009-0081565).

Acknowledgment

We thank Dr. H.-S. Ee for helpful discussions during the analysis of simulation results.